



King's Research Portal

DOI:

[10.1073/pnas.1517437113](https://doi.org/10.1073/pnas.1517437113)

Document Version

Peer reviewed version

[Link to publication record in King's Research Portal](#)

Citation for published version (APA):

Sengel, J. T., & Wallace, M. I. (2016). Imaging the dynamics of individual electropores. *Proceedings of the National Academy of Sciences*, 113(19), 5281-5286. <https://doi.org/10.1073/pnas.1517437113>

Citing this paper

Please note that where the full-text provided on King's Research Portal is the Author Accepted Manuscript or Post-Print version this may differ from the final Published version. If citing, it is advised that you check and use the publisher's definitive version for pagination, volume/issue, and date of publication details. And where the final published version is provided on the Research Portal, if citing you are again advised to check the publisher's website for any subsequent corrections.

General rights

Copyright and moral rights for the publications made accessible in the Research Portal are retained by the authors and/or other copyright owners and it is a condition of accessing publications that users recognize and abide by the legal requirements associated with these rights.

- Users may download and print one copy of any publication from the Research Portal for the purpose of private study or research.
- You may not further distribute the material or use it for any profit-making activity or commercial gain
- You may freely distribute the URL identifying the publication in the Research Portal

Take down policy

If you believe that this document breaches copyright please contact librarypure@kcl.ac.uk providing details, and we will remove access to the work immediately and investigate your claim.

1 **Title:** Imaging the dynamics of individual electropores

2 **Authors:** Jason T. Sengel,¹ Mark I. Wallace^{*1,2}

3 ^{*}Correspondence to: mark.wallace@chem.ox.ac.uk

4 **Affiliations:**

5 ¹University of Oxford, Department of Chemistry, Chemistry Research Laboratory, 12
6 Mansfield Road, Oxford, OX1 3TA, U.K.

7 ²King's College London, Department of Chemistry, Britannia House, 7 Trinity Street,
8 London, SE1 1DB, U.K.

9 **Abstract**

10 Electroporation is a widely used technique to permeabilize cell membranes. Despite its
11 prevalence, our understanding of the mechanism of voltage-mediated pore formation
12 is incomplete; methods capable of visualizing the time-dependent behavior of
13 individual electropores would help improve our understanding of this process. Here,
14 using optical single-channel recording we track multiple isolated electropores in real
15 time in planar droplet interface bilayers. We observe individual, mobile defects that
16 fluctuate in size, exhibiting a range of dynamic behaviors. We observe fast (25 s^{-1})
17 and slow (2 s^{-1}) components in the gating of small electropores, with no apparent
18 dependence on the applied potential. Further, we find that electropores form
19 preferentially in the liquid disordered phase. Our observations are in general
20 supportive of the hydrophilic toroidal pore model of electroporation, but also reveal
21 additional complexity in the interactions, dynamics and energetics of electropores.

22

1 **Significance Statement**

2 Transient permeabilization of the cell membrane is needed to introduce genes and
3 drugs into cells, and electroporation (the physical breakdown of a bilayer membrane
4 under an external electric field) is the most common method to achieve this. By
5 applying an electric field to an artificial lipid bilayer we have been able to visualize
6 the presence of individual electropores in the bilayer. We exploit droplet interface
7 bilayers, (formed from the contact between an aqueous droplet and a hydrogel surface
8 immersed in a phospholipid/oil solution) to provide simultaneous single-channel
9 electrical recording and fluorescence imaging of the bilayer.

10

1 \body

2 **Introduction**

3 Maintenance of an intact cell membrane is vital for cell viability; it provides the
4 barrier that prevents cell lysis and controls permeability to the external environment.

5 However, intentional transient permeabilization of the membrane is also exploited as
6 a means to introduce genes or drugs into an organism, and targeted permanent
7 disruption of plasma membranes is an effective means to eliminate specific cells.¹⁻³

8 Electroporation (or electropermeabilization) - the physical breakdown of a bilayer
9 membrane under an external electric field - is a long-standing, popular method used to
10 control the integrity of a cell membrane. Since its discovery and the first
11 investigations in the 1960s and '70s,^{4,5} electroporation has been used in a wide range
12 of applications, including gene transfection,⁶ wound and water sterilization,^{7,8} tumor
13 ablation,^{9,10} electrochemotherapy,^{11,12} and transdermal drug delivery.¹³ Furthermore,
14 links to defibrillation damage have been highlighted.¹⁴

15 **Toroidal pore model.** The transient aqueous pore hypothesis provides the basis of
16 our current understanding of electroporation (Fig. 1). In this model the kinetics of
17 pore formation are governed by the transition over an energy barrier E^* created by the
18 intersection of potentials corresponding to two distinct pore configurations: (1) a
19 hydrophobic pore, where the lipids are simply parted with respect to an intact
20 membrane, and (2) a hydrophilic, toroidal pore.¹⁵ In this work, when describing a
21 toroidal pore, we refer to a conductive pore, with the lumen lined and stabilized by
22 lipid head groups (Fig. 1a). At small radii, hydrophilic pores reside within a local
23 energy minimum;¹⁶ at large radii, there exists a local maximum (with associated
24 critical radius r_c), beyond which a pore may grow indefinitely. The application of a

1 transmembrane potential modifies the free energy of the hydrophilic pore such that its
2 free energy, along with this barrier, are reduced (Fig. 1b). At a critical potential V_c this
3 barrier to unbounded pore expansion is lost and the defect grows until the bilayer is
4 destroyed.

5 **Previous imaging of electropores.** Theory and simulation have provided a rich
6 source of predictions regarding the properties of electropores. For example, molecular
7 dynamics simulations have predicted the evolution of hydrophilic pores takes place
8 from an initial membrane-spanning water file.¹⁷⁻¹⁹ However, there is a conspicuous
9 mismatch between this level of predictive power and the information yielded by
10 experiment.

11 Studies visualizing the presence of electropores are extremely limited. Techniques
12 such as rapid freezing of electroporated erythrocytes²⁰ have provided snapshots
13 suggestive of pore formation, but these have been disputed.²¹ The transient nature and
14 small size of electropores place significant limitations on the measurement of
15 electropore dynamics, and more fundamentally on their direct detection. Electrical
16 single-channel recording (SCR) can resolve these dynamics at high time
17 resolution,^{22,23} however SCR is limited in that it can only detect the total current
18 across the membrane, and is thus unable to resolve whether conductance events are
19 due to single or multiple permeabilization events. Indeed, the most common
20 characteristic for electroporation in SCR would be a “noisy” trace that precedes
21 bilayer rupture (see Fig. S5a, lower).

22 A better insight into electropore formation would be provided by methods capable of
23 observing the dynamics of electropore formation in real time. Few dynamic
24 experimental imaging studies of these defects exist. Pioneering work in giant
25 unilamellar vesicles (GUVs) has led to methods for assessing line tension, studying

1 pore closure and formation times, and the dynamics of solute flow between the
2 internal and external volumes.^{24,25} For example, GUVs have been used to show
3 transport across a membrane can be achieved by an electroporation pulse only 10 ns
4 in duration.²⁶ However, many of these systems typically examine small numbers of
5 large, microscopic pores, much larger than the nanoscopic pores observed in cell
6 systems (20-120 nm),²⁰ predicted by MD simulations^{17,19} and implied by cellular
7 uptake assays.²⁷

8 Here we seek to improve our experimental understanding of electroporation by
9 exploiting optical single-channel recording (oSCR)^{28,29} to image individual voltage-
10 induced defects in a lipid membrane by detecting a fluorescent signal proportional to
11 the flux of Ca^{2+} flowing through a pore. Very recently, we detected electroporation
12 events using fluorescence signals generated by K^+ ionic flux.³⁰ Although this work
13 showed electropores formed under the same applied potentials as reported here, it was
14 limited by the slow response and poor sensitivity of K^+ -responsive fluorophores. In
15 this work the enhanced sensitivity of fluorogenic Ca^{2+} -sensitive dyes allows us to
16 characterize electroporation kinetics in detail.

17 We previously developed droplet interface bilayers³¹ (DIBs, Fig. 2a) to create highly
18 stable, size-adjustable artificial bilayers that are straightforward to image using total
19 internal reflection fluorescence (TIRF) microscopy, providing imaging that is
20 sensitive to signals originating at the bilayer. DIBs are formed when a planar hydrogel
21 surface and an aqueous droplet are brought into contact in a lipid-in-oil solution.

22 Using DIBs, we visualize the ionic flux through nanoscopic membrane defects in real
23 time over a large area ($\geq 14000 \mu\text{m}^2$). We classify electropore behavior and compare
24 it to the current model, helping bridge the gap between theory, simulation and
25 experiment.

1 **Results**

2 **Fluorescence imaging of electroporation.** Diphytanoyl phosphatidylcholine
3 (DPhPC) bilayers were formed and subjected to DC potentials (see Supplementary
4 Text for full experimental details). Upon application of a potential difference of ≥ 90
5 mV, individual electropores form and calcium is driven from the substrate into the
6 droplet where it is bound by the fluorogenic Ca^{2+} indicator dye Fluo-8. Individual
7 electropores are visualized as isolated bright spots in the bilayer (Fig. 2b). oSCR
8 enables the location and conductance from many individual pores to be monitored in
9 parallel. For a DIB containing a single pore, there is direct correlation between
10 electrical and fluorescence signals (Fig. 2c); for multiple pores, the sum fluorescence
11 trace corresponds to the total ionic current across the bilayer (Fig. S2). This
12 decomposition of multiple signals is inaccessible in a direct electrical recording.

13 **I-V response.** We first examined the ensemble current-voltage (I-V) response (Fig.
14 S3). As expected, at low potentials the bilayer is essentially non-conducting ($7.99 \pm$
15 $0.27 \times 10^{10} \Omega$). Current fluctuations appear above ~ 100 mV (onset 111 ± 41 mV) and
16 the I-V curve becomes increasingly nonlinear until breakdown. V_c was found to be
17 224 ± 39 mV ($n = 17$) when the agarose and droplet contained 1.5 M KCl, and $272 \pm$
18 29 mV ($n = 7$) when the agarose contained 750 mM CaCl_2 . The apparent stabilizing
19 effect of calcium is perhaps a result of the divalent cation having a stronger
20 electrostatic interaction with the lipid head groups than K^+ , as has been reported in
21 other membrane systems.²²

22 The I-V response is mirrored in the fluorescence data (see Fig. S4), however, only by
23 using oSCR are we now able to attribute this to an increase in both the number of
24 pores and their size (Fig. 3), rather than solely by the expansion of a single pore. In
25 examining the distribution of fluorescence intensities from electropores as a function

1 of applied voltage for a single pore, Fig. 3b, we observe a broadening of the
2 distribution of pore intensities, with a mean that increases with the applied potential.
3 This observation is consistent with a broadening of the local energy minimum at
4 higher applied potentials (Fig. 1b).¹⁶ We also note that for an ensemble of pores (Fig.
5 3c), a population of small pores remains even at high potentials, as can also be seen in
6 Fig. 3a.

7 **Pore taxonomy.** Individual electropore signals fluctuate in a variety of modes (Fig.
8 S5): switching between quiescent and noisy states; rapid rises to high currents; heavy
9 current fluctuations; long periods at stable radii; or the sudden collapse of a pore.

10 Electropore gating and extended opening have been previously reported using
11 electrical recording,^{5,22,23} however here, by isolating individual oSCR signals, we are
12 able to extend observation of these phenomena to higher potentials, where the
13 individual signals would be obscured in a purely electrical measurement. We have
14 observed that all of these modes can occur at elevated potentials, with no apparent
15 favor of one mode over another.

16 Visualization of pores during the application of potential across the bilayer allows us
17 to confirm when there is a single pore present. This often occurs at low (80-110 mV)
18 potentials, and we may determine the conductance of these defects and thus estimate
19 our sensitivity. Our oSCR observations of isolated electropores indicate that
20 conductances as small as 400 pS may be (optically) detected, a sensitivity over five
21 times better than obtained using potassium-sensitive dyes.³⁰ This current is similar in
22 magnitude to the current measured directly at the onset of electroporation where
23 presumably only a single electropore is also present (see Fig. S5a, upper).

24 Approximating an electropore as a cylindrical defect (see Supplementary Text) we
25 obtain an approximate pore radius of 0.22 nm for the smallest pores (those detected at

1 the onset of electroporation). This value will be an underestimate as the field
2 experienced in the region of the pore will be reduced upon its formation,^{32,33} however
3 it supports previous suggestions that the smallest electrically conductive pores are
4 those able to accommodate at least a single file of ions. This value is also on the order
5 of the smallest pores found in experimental and theoretical studies.^{19,27,34-36}

6 **Electropore diffusion.** Individual, diffusing electropores can be tracked within the
7 membrane (Fig. 4a). Mobile pores were generally small and exhibited a broad
8 distribution of lateral diffusion coefficients (D_{lat}) (Fig. 4b) with a mean value of 0.67
9 $\pm 0.58 \mu\text{m}^2 \text{s}^{-1}$ (max: $2.7 \mu\text{m}^2 \text{s}^{-1}$; min: $0.037 \mu\text{m}^2 \text{s}^{-1}$). The lateral diffusion coefficient
10 of these pores showed no obvious correlation with applied potential.

11 **Phase-dependence of electroporation.** Molecular dynamics simulations predict that
12 electroporation is favored in lipid regions of greater disorder.³⁷ We electroporated
13 phase-separated DIBs using two ternary mixtures, diphytanoyl phosphatidylcholine/
14 dipalmitoyl phosphoglycerol/cholesterol and diphytanoyl phosphatidylcholine/brain-
15 sphingomyelin/cholesterol (both molar ratio 1:1:1) which exhibited liquid ordered
16 (L_o) and liquid disordered (L_d) phase coexistence. Domains were visualized using 1
17 mol% of the lipophilic dye DiI, which partitions into the liquid disordered phase.
18 Figure 4c shows an median-averaged image from such an experiment, overlaid with
19 trajectories of electropores diffusing in the membrane (see also Supp. Fig. S6 &
20 Movies S4 & S5). Pores are seen to move within the L_d phase, moving between but
21 not into L_o domains.

22 **Pore closure and bilayer rupture.** Experiments carried out in cells have indicated
23 that some pores can remain open for hundreds of seconds,^{27,38,39} whereas closure is
24 typically in the nano- to microsecond range in simulations.^{19,33} Within the time

1 resolution of our experiments (16 ms) we observe pores that close immediately upon
2 removal of the applied potential.

3 Uncertainty exists as to whether bilayer rupture is a result of a single expanding pore,
4 or a collection of smaller defects.^{25,40} Figure 5a shows consecutive frames during DIB
5 breakdown: we observe bilayer rupture to only take place via a single electropore.

6 During the growth of this critical defect, other pores shrink and seal, likely as the
7 sudden increase in conductance relaxes the potential across the membrane. Once
8 started, the rupture process cannot be arrested. These observations support the
9 transient aqueous pore model where once a defect above the critical radius r_c is
10 formed, there is rapid and uncontrolled expansion of the pore.^{15,16} We note that the
11 rupture patterns we observe (Fig. 5a, lower row) are similar to the floral instability
12 patterns seen in rupturing multi-lamellar vesicles.⁴¹

13 In phase-separated bilayers, the L_0 boundary delimiting the disordered regions in
14 which electropores can form (Fig. S6b) does not appear to restrict the expansion of
15 the pore at elevated potentials; rupture occurs from one disordered region and
16 proceeds to destroy the whole bilayer.

17 **Interactions between electropores.** A further question that has been raised is
18 whether electropores are able to coalesce.^{25,42} We only observe isolated pores and do
19 not observe electropore coalescence in our experiments. Additionally, we have
20 observed anti-correlation in pore currents (Fig. 5b), either when small pores are in
21 close proximity (several 10s of micrometers), or when a critical pore exists within the
22 membrane (see Fig. 5a). Such behavior would be consistent with modulation of either
23 the local electric field or membrane surface tension by the presence of other pores.

1 **Gating kinetics.** Large pores were observed to persist throughout the duration of our
2 experiments, however at the onset of electroporation, we observe discrete fluctuations
3 in pore radius. This can be maintained for periods of up to several hundred seconds,
4 and can be observed in both electrical and fluorescence recordings (uppermost traces,
5 Fig. S5a and b). Given that this behavior arises at the onset of defect formation, we
6 attribute this type of conductance to the opening and closing of the smallest possible
7 pore. This is supported by the value of our estimation for the radii of these defects. To
8 gain a more detailed understanding of the energetic barrier to pore formation we
9 examined these gating kinetics in detail. Electropores were imaged over a range of
10 potentials, with a transition between open and closed states defined by a threshold set
11 at 3 times the standard deviation of the background intensity (Fig. 6a). Pore lifetimes
12 were best fit by double exponentials (Fig. 6b), compared with single or stretched
13 exponentials. Results from analysis of ≥ 1900 pores are shown in Fig. 6c; the
14 prominent feature is that these characteristic lifetimes are essentially invariant with
15 the applied potential.

16 **Discussion**

17 oSCR has enabled us to make a wide range of quantitative measurements
18 characterizing electropore behavior. This work is unique in reporting the real-time
19 dynamics of isolated electropores within an ensemble of defects. Electrical
20 measurements of electroporation typically show noisy, poorly resolved features; we
21 are able to attribute this noisy fluctuating signal to an ensemble of individual
22 permeabilization events in the bilayer, rather than a more generalized mechanism of
23 bilayer disruption.

24 The diffusion of electropores, along with their rapid fluctuation in conductance,
25 confirms that their structure is highly dynamic. Across the range of applied potentials,

1 the majority of tracked pores were of a similar size; in this case the apparent lack of
2 correlation between the diffusion coefficient and the applied potential may be
3 expected as the electric field around a pore is predicted to be radially isotropic.³²
4 However, the sample size is small ($n = 46$), and any presumed relationship between
5 V_{applied} (hence pore size) and D_{lat} may be further complicated by the rapidly
6 fluctuating pore radius.

7 Examining the distribution of oSCR intensities as function of potential (Fig. 3c)
8 shows that a population of smaller pores is retained as the potential is raised.
9 Although the distribution becomes less dominated by them, at elevated voltages the
10 smallest observable defects remain across the full range of the applied potential
11 difference. This behavior is consistent with a toroidal pore model in which the
12 crossing point between the hydrophobic and hydrophilic energy surfaces (Fig. 1b) is
13 not susceptible to a change in the applied potential. The broadening of the oSCR
14 intensity distribution (and hence pore radius) as the applied potential increases
15 supports the common depiction of hydrophilic energy curves: the potential well that
16 supports hydrophilic pores widens and shifts to larger radii at elevated potentials.

17 Individual electropores can remain open for 10s to 100s of seconds under an applied
18 voltage, however the proportion of these instances relative to the rapidly gating
19 electropores is low. As a result, the data on fluctuating pores reports on the kinetics
20 associated with the transition over the hydrophilic-hydrophobic energy barrier: the
21 open time represents the depth of the energy well corresponding to a hydrophilic pore;
22 the closed time corresponds to the height of the barrier for hydrophilic pore formation.

23 The independence of open times on applied potential (Fig. 6c, upper) implies that in
24 our experiments there is no significant deepening of the hydrophilic pore well with
25 applied potential. A rise in potential does broaden this local minimum, granting access

1 to a greater range of pore radii (Fig. 3b and c), but we do not observe that pores at
2 these higher potentials are more stable. The suggestion that the applied potential does
3 not influence the kinetics of pore opening is consistent with previous work by
4 Wilhelm *et al.*⁴⁰

5 The closed time similarly does not vary with increasing potential, implying that the
6 height of the energy barrier to hydrophilic pore formation is also relatively constant,
7 i.e. the point where hydrophobic and hydrophilic potentials cross, E^* , is insensitive to
8 applied potential. (This is further supported by our observation of small electropores
9 at high potentials.) This is consistent with the proposed mechanism for the transition
10 between a hydrophobic and a hydrophilic pore: the lipid rearrangement is
11 predominantly driven by the minimization of the unfavorable interaction between
12 water and the tail groups. Similarly, collapse of a conducting defect will always
13 require the coming together of the water-lined toroidal pore walls, and the physical
14 forces associated with this, along with those governing the transition of lipids back to
15 a parallel, unperturbed bilayer arrangement, are unlikely to be greatly modulated by
16 the potential. The idea that the crossing point between these potentials exists at a fixed
17 location in terms of energy and radius has been hypothesized previously.³⁶

18 The reason for the open and closed times exhibiting two components is less clear. The
19 histograms used to determine the pore lifetimes in Fig. 6 contain data from more than
20 1900 electropores, however, analysis of individual pores shows that single pores also
21 exhibit double exponential behavior (Fig. S7). Each defect appears able to exist in
22 either a short or long-lived open or closed state. We tentatively attribute the longer
23 timescales, $\tau_{2,\text{open}} \approx 400$ ms and $\tau_{2,\text{closed}} \approx 600$ ms, to the process of hydrophilic pore
24 opening and closure, respectively. The observation that $\tau_{2,\text{closed}} > \tau_{2,\text{open}}$ is consistent
25 with the barrier to conductive pore formation being larger than the barrier to pore

1 collapse. The shorter times ($\tau_{1,\text{open}}$, $\tau_{1,\text{closed}} \approx 30\text{-}40$ ms) have a less obvious origin,
2 and are not supported by the simple toroidal pore model. Bimodal rates for both
3 opening and closing would be consistent with a number of different kinetic models,
4 for example, a single closed state in equilibrium with two distinct open states.
5 Molecular dynamics simulations have suggested that brief pore openings may be the
6 result of conductive hydrophobic pores.⁴³ However, this would require such a
7 conductive hydrophobic pores to be long-lasting, with no favorable transition to the
8 hydrophilic toroidal state. Alternatively, these lifetimes may be the result of brief
9 (hydrophilic) openings as the potential only just overcomes E^* , in which case the pore
10 opens, reduces the local electric field, and rapidly closes. Future work will help move
11 beyond this speculation as to the nature of these kinetics.

12 Our observations point towards established defects influencing the nature of new
13 ones: anti-correlation in pore fluctuations and the relaxation of the electrical stress on
14 the membrane when a very large pore exists (Fig. 5; see also Supplementary Movies
15 S2 & S3) are evidence of this. These factors are very likely the cause of the range of
16 fluctuation regimes we observe (Fig. S5), and may contribute to the maintenance of
17 small pores at higher potentials (Fig. 3c). The way in which biological membranes
18 dissipate or augment these local tensile or electrical stresses during electroporation is
19 therefore of great interest if we are to further understand this phenomenon *in vivo*.

20 **Limitations**

21 The events we detect do not provide a direct measurement of pore size: the
22 fluorescent events corresponding to the ‘cloud’ of ion flux flowing through each pore
23 is larger than the pore itself. Although we can resolve the locations of individual pores
24 to within a few tens of nanometers, we cannot image their structure directly.
25 Furthermore, optical detection of electropores is unavoidably constrained by the

1 diffraction limit, and, although unlikely,⁴² if multiple pores exist within the
2 diffraction-limited point spread function (FWHM = 0.59 μm) they will be essentially
3 unresolved.

4 The time resolution of our current experiments (16 ms) also limits our ability to
5 investigate electroporation kinetics. Such a restriction means that we are unable to
6 observe electropore dynamics under the (typically) nano- to microsecond pulsed AC
7 protocols that are typically used to electroporate cells. These rapid, transient
8 applications of potential are designed primarily to reduce thermal damage that would
9 otherwise kill the cell. However, in our experiments, with a small number of isolated
10 pores over the bilayer area, we observe no measureable temperature changes
11 associated with current flow.

12 Lastly, the presence of a supporting agarose substrate might potentially perturb
13 electropore kinetics, however our observations of Brownian diffusion of electropores
14 and bimodal kinetics independent of diffusion (Fig. S7) imply that any effect of the
15 substrate is minor.

16 **Summary**

17 Our results are in support of the hydrophilic toroidal pore model, however the kinetics
18 we resolve are not completely explained by this simple scheme. Under an electric
19 field, electropores appear and disappear within the membrane in a stochastic manner,
20 and exhibit constantly fluctuating radii. Pores become more numerous and fluctuate
21 around greater radii as the applied potential is increased, as is consistent with our
22 current understanding. Electroporation in this system appears not to be characterized
23 by a single behavior, but by a range of fluctuation regimes. These observations point
24 towards more complex interactions between electropores, indicating that local

1 variations in the electric field or surface tension owing to pores already present limit
2 the size of newly formed defects.

3 The ability to decompose the total current across the bilayer due to electroporation
4 into the component contribution of individual electropores has enabled us to shed
5 further light on the physical mechanism that controls this important phenomenon. The
6 next steps must be to bridge the gap between the insights afforded by these *in vitro*
7 models, and the realities of electroporation *in vivo*.

8 **Experimental**

9 **Materials.** Stocks of 1,2 diphytanoyl-*sn*-glycero-3-phosphocholine (DPhPC), 1,2-
10 dipalmitoyl-*sn*-glycero-3-phosphoglycerol (DPPG), brain sphingomyelin (bSM) and
11 cholesterol (all Avanti Polar Lipids) were stored in chloroform at -20 °C. 8.7 mg mL⁻¹
12 solutions of lipid in hexadecane were produced from these stocks before each
13 experiment. All aqueous solutions were prepared using doubly-deionised 18.2 MΩ cm
14 MilliQ water. Low-melt agarose (Sigma-Aldrich) solutions were freshly prepared
15 each day and kept at 90°C to ensure homogeneity. Potassium chloride solutions were
16 buffered with 10 mM HEPES, adjusted with potassium hydroxide, treated with
17 Chelex resin (200-400 mesh, BioRad) in order to remove divalent cations, and filtered
18 using a 0.22 μm Steriflip disposable filter (Millipore Corporation). All experiments
19 were carried out within purpose-machined PMMA devices with sixteen distinct
20 wells,⁴⁴ enabling multiple bilayers to be imaged using a single device. Calcium-
21 sensitive Fluo-8 fluorescent dye (AAT Bioquest) was prepared as a 1 mg mL⁻¹ stock
22 solution in distilled water and stored at -20 °C. All other chemicals were purchased
23 from Sigma-Aldrich. Conductivity of solutions were measured at 21.1°C using a
24 calibrated (12.88 mS cm⁻¹) Mettler Toledo FG3 meter with LE703 probe. The

1 conductivities were determined to be: 1.5 M KCl, 10 mM HEPES: 144 mS cm⁻¹; 750
2 mM CaCl₂, 10 mM HEPES: 99.5 mS cm⁻¹.

3 **Device preparation and experimental setup.** DIBs were prepared as described
4 previously.⁴⁴ Briefly, plasma-cleaned coverslips were spin-coated with 0.75 % (w/v)
5 aqueous agarose, then affixed to the device. This was subsequently filled with 2 %
6 (w/v) hydrating agarose solution containing buffered KCl or CaCl₂. This hydrates (but
7 does not cover) the substrate agarose by surrounding each well. Lipid-in-oil (8.7 mg
8 mL⁻¹ in hexadecane) was applied to the wells. After an incubation period to allow a
9 monolayer to form (~15-30 mins), aqueous droplets in the same lipid-in-oil solution
10 were added to the wells, forming a bilayer with the substrate under gravity. Prepared
11 devices were placed within a Faraday cage on an inverted microscope (Eclipse TiE,
12 Nikon). Ag/AgCl electrodes were inserted into the hydrating agarose and the droplet,
13 and connected to an Axopatch 200B patch-clamp amplifier (Molecular Devices) in
14 voltage-clamp mode. DIBs were observed using a 60x TIRF oil objective (Nikon).
15 Fluo-8 was excited by fibre-launched 473 nm CW laser radiation (~4 mW at fibre
16 output) and imaged on an electron-multiplying CCD (iXon3 897, Andor). All
17 experiments were conducted at room temperature. (Further detail on the experimental
18 setup may be found in the Supplementary Text.)

19 **Phase-separated DIBs.** Bilayers were prepared as described, using mixtures of either
20 DPhPC:DPPG:cholesterol or DPhPC:bSM:cholesterol (1:1:1 molar, total lipid
21 concentration 8.7 mg mL⁻¹). The lipid-in-oil mixture also contained 1 mol% of the
22 lipophilic dye DiI. After the droplets were added to the device wells, the device was
23 incubated at 45 °C for 20 minutes to ensure lipid mixing. Both Fluo-8 and DiI were
24 excited by the 473 nm laser, and the fluorescence signal recorded on an electron-
25 multiplying CCD (iXon+, Andor).

1 **Data analysis.** Spot fluorescence was analyzed by examining a circular region of
2 interest around each spot. The mean pixel intensity of this region versus time was then
3 calculated (Figs. 2 and 5). For all other figures, tracking of pores was carried out
4 using the Trackmate plugin in Fiji,⁴⁵ before Gaussian fitting. Further details are given
5 in the Supplementary Text. All errors are quoted as plus-minus one standard
6 deviation.

7 **Acknowledgements**

8 The authors thank John S. H. Danial for aid in preparing phase-separated bilayers, and
9 the ERC for providing the funding for this research (CoSMiC 106913).

10 **Author contributions**

11 J.T.S. and M.I.W. designed the experiments and discussed the results; J.T.S. carried
12 out the experimental work and data analysis. J.T.S. and M.I.W. prepared the
13 manuscript.

14 **Competing financial interests**

15 The authors declare no competing financial interest.

16 **References**

- 17 1. Haberl S, Miklavčič D, Sersa G, Frey W, Rubinsky B (2013) Cell membrane
18 electroporation - Part 2: the applications. *IEEE Electr Insul Mag* 29(1):29–37.
- 19 2. Mahnič-Kalamiza S, Vorobiev E, Miklavčič D (2014) Electroporation in Food
20 Processing and Biorefinery. *J Membr Biol* 247(12):1279–1304.
- 21 3. Yarmush ML, Golberg A, Serša G, Kotnik T, Miklavčič D (2014)
22 Electroporation-Based Technologies for Medicine: Principles, Applications, and
23 Challenges. *Annu Rev Biomed Eng* 16(1):295–320.
- 24 4. Stämpfli R, Willi M (1957) Membrane potential of a Ranvier node measured
25 after electrical destruction of its membrane. *Experientia* 13(7):297–298.

- 1 5. Yafuso M, Kennedy SJ, Freeman AR (1974) Spontaneous conductance changes,
2 multilevel conductance states and negative differential resistance in oxidized
3 cholesterol black lipid membranes. *J Membr Biol* 17(1):201–212.
- 4 6. Gothelf A, Gehl J (2012) What you always needed to know about
5 electroporation based DNA vaccines. *Hum Vaccines Immunother* 8(11):1694–
6 1702.
- 7 7. Golberg A et al. (2015) Pulsed Electric Fields for Burn Wound Disinfection in a
8 Murine Model. *J Burn Care Res* 36(1):7–13.
- 9 8. Liu C et al. (2014) Static Electricity Powered Copper Oxide Nanowire
10 Microbicidal Electroporation for Water Disinfection. *Nano Lett* 14(10):5603–
11 5608.
- 12 9. Golberg A, Yarmush ML (2013) Nonthermal Irreversible Electroporation:
13 Fundamentals, Applications, and Challenges *IEEE Trans Biomed Eng*
14 60(3):707–714.
- 15 10. Jiang C, Davalos RV, Bischof JC (2015) A Review of Basic to Clinical Studies
16 of Irreversible Electroporation Therapy. *IEEE Trans Biomed Eng* 62(1):4–20.
- 17 11. Mali B, Jarm T, Snoj M, Sersa G, Miklavčič D (2013) Antitumor effectiveness of
18 electrochemotherapy: A systematic review and meta-analysis. *Eur J Surg Oncol*
19 *EJSO* 39(1):4–16.
- 20 12. Cadossi R, Ronchetti M, Cadossi M (2014) Locally enhanced chemotherapy by
21 electroporation: clinical experiences and perspective of use of
22 electrochemotherapy. *Future Oncol* 10(5):877–890.
- 23 13. Schoellhammer CM, Blankschtein D, Langer R (2014) Skin permeabilization for
24 transdermal drug delivery: recent advances and future prospects. *Expert Opin*
25 *Drug Deliv* 11(3):393–407.
- 26 14. Dossdall DJ, Fast VG, Ideker RE (2010) Mechanisms of Defibrillation. *Annu Rev*
27 *Biomed Eng* 12(1):233–258.
- 28 15. Abidor, IG et al. (1979) Electric breakdown of bilayer lipid membranes I. The
29 main experimental facts and their qualitative discussion. *Bioelectrochem*
30 *Bioenerg* 6(1):37–52.
- 31 16. Neu JC, Krassowska W (1999) Asymptotic model of electroporation. *Phys Rev E*
32 59(3):3471–3482.
- 33 17. Tieleman DP (2004) The molecular basis of electroporation. *BMC Biochem*
34 5(1):1–12.
- 35 18. Tarek M (2005) Membrane Electroporation: A Molecular Dynamics Simulation.
36 *Biophys J* 88(6):4045–4053.

- 1 19. Levine ZA, Vernier PT (2010) Life Cycle of an Electropore: Field-Dependent
2 and Field-Independent Steps in Pore Creation and Annihilation. *J Membr Biol*
3 236(1):27–36.
- 4 20. Chang DC, Reese TS (1990) Changes in membrane structure induced by
5 electroporation as revealed by rapid-freezing electron microscopy. *Biophys J*
6 58(1):1-12.
- 7 21. Chernomordik LV (1992) Electropores in Lipid Bilayers and Cell Membranes.
8 *Guide to electroporation and electrofusion*. (Academic Press, San Diego)
- 9 22. Heimburg T (2010) Lipid ion channels. *Biophys Chem* 150(1-3):2–22.
- 10 23. Melikov KC et al. (2001) Voltage-induced nonconductive pre-pores and
11 metastable single pores in unmodified planar lipid bilayer. *Biophys J*
12 80(4):1829–1836.
- 13 24. Riske KA, Dimova R (2005) Electro-Deformation and Poration of Giant Vesicles
14 Viewed with High Temporal Resolution. *Biophys J* 88(2):1143–1155.
- 15 25. Portet T, Dimova R (2010) A New Method for Measuring Edge Tensions and
16 Stability of Lipid Bilayers: Effect of Membrane Composition. *Biophys J*
17 99(10):3264–3273.
- 18 26. Breton M, Delemotte L, Silve A, Mir LM, Tarek M (2012) Transport of siRNA
19 through lipid membranes driven by nanosecond electric pulses: an experimental
20 and computational study. *J Am Chem Soc* 134(34):13938-13941
- 21 27. Saulis G, Saulè R (2012) Size of the pores created by an electric pulse:
22 Microsecond vs millisecond pulses. *Biochim Biophys Acta - Biomembr*
23 1818(12):3032-3039
- 24 28. Demuro A, Parker I (2004) Imaging the Activity and Localization of Single
25 Voltage-Gated Ca²⁺ Channels by Total Internal Reflection Fluorescence
26 Microscopy. *Biophys J* 86(5):3250–3259.
- 27 29. Shuai J, Parker I (2005) Optical single-channel recording by imaging Ca²⁺ flux
28 through individual ion channels: theoretical considerations and limits to
29 resolution. *Cell Calcium* 37(4):283–299.
- 30 30. Szabo M, Wallace, MI (2015) Imaging potassium-flux through individual
31 electropores in droplet interface bilayers. *Biochim Biophys Acta - Biomembr*
32 doi:10.1016/j.bbamem.2015.07.009
- 33 31. Bayley H et al. (2008) Droplet interface bilayers. *Mol Biosyst* 4(12):1191–1208.
- 34 32. Neu JC, Smith KC, Krassowska W (2003) Electrical energy required to form large
35 conducting pores. *Bioelectrochemistry Amst Neth* 60(1-2):107-114.
- 36 33. Smith KC, Sona RS, Gowrishankara TR, Weaver JC (2014) Emergence of a large
37 pore subpopulation during electroporating pulses. *Bioelectrochem* 100:3–10.

- 1 34. Dimitrov V, Kakorin S, Neumann E (2013) Transient oscillation of shape and
2 membrane conductivity changes by field pulse-induced electroporation in nano-
3 sized phospholipid vesicles. *Phys Chem Chem Phys* 15: 6303-6322.
- 4 35. Ho MC, Casciola M, Levine ZA, Vernier PT (2013) Molecular Dynamics
5 Simulations of Ion Conductance in Field-Stabilized Nanoscale Lipid
6 Electropores. *J Phys Chem B* 117 (39):11633–11640.
- 7 36. Glaser RW, Leikin SL, Chernomordik LV, Pastushenko VF, Sokirko AI (1988)
8 Reversible electrical breakdown of lipid bilayers: formation and evolution of
9 pores. *Biochim Biophys Acta* 940(2):275–287.
- 10 37. Reigada R (2014) Electroporation of heterogeneous lipid membranes. *Biochim*
11 *Biophys Acta - Biomembr* 1838(3):814–821.
- 12 38. Shirakashi R, Sukhorukov VL, Tanasawa I, Zimmermann U (2004) Measurement
13 of the permeability and resealing time constant of the electroporated mammalian
14 cell membranes. *Int J Heat Mass Transfer* 47(21):4517–4524.
- 15 39. Pucihar G, Kotnik T, Teissié J, Miklavčič D (2007) Electropermeabilization of
16 dense cell suspensions. *Eur Biophys J* 36(3):173-185.
- 17 40. Wilhelm C, Winterhalter M, Zimmermann U, Benz R (1993) Kinetics of pore
18 size during irreversible electrical breakdown of lipid bilayer membranes.
19 *Biophys J* 64(1):121-128.
- 20 41. Gözen I et al. (2010) Fractal avalanche ruptures in biological membranes. *Nat*
21 *Mater* 9(11):908–12.
- 22 42. Freeman SA, Wang MA, Weaver JC (1994) Theory of electroporation of planar
23 bilayer membranes: predictions of the aqueous area, change in capacitance, and
24 pore-pore separation. *Biophys J* 67(1):42-56.
- 25 43. Dehez F, Delemotte L, Kramar P, Miklavčič D, Tarek M (2014) Evidence of
26 Conducting Hydrophobic Nanopores Across Membranes in Response to an
27 Electric Field. *J Phys Chem C* 118(13):6752–6757.
- 28 44. Leptihn S et al (2013) Constructing droplet interface bilayers from the contact of
29 aqueous droplets in oil. *Nat Protoc* 8(6):1048–1057.
- 30 45. Schindelin J et al (2012) Fiji: an open-source platform for biological-image
31 analysis. *Nat Methods* 9(7):676–682.
- 32 46. Högbom JA (1974) Aperture Synthesis with a Non-Regular Distribution of
33 Interferometer Baselines. *Astron Astrophys Suppl Ser* 15:417-426.
- 34 47. Cronin B, de Wet B, Wallace MI (2009) Lucky Imaging: Improved Localization
35 Accuracy for Single Molecule Imaging. *Biophys J* 96(7):2912–2917.

36 **Figure Legends**

1 **Fig. 1: The transient aqueous pore hypothesis.** (a) The sequence of lipid
2 rearrangements that lead to a conductive (hydrophilic, or toroidal) pore. Formation
3 proceeds from the unperturbed membrane (i) via a non-conducting hydrophobic pore
4 generated by the parting of lipids but involving no molecular reorientation (ii). At
5 sufficiently large radii, however, lipids rearrange and headgroups line the pore lumen
6 (iii). (b) Electropore energy landscape highlighting the hydrophobic and hydrophilic
7 pore free energies (dashed and solid lines respectively) using the equations and
8 parameter values from ref. 16, which are those commonly used in theoretical
9 electroporation literature. Their intersection is indicated at *; we refer to this energy
10 barrier as E^* . The grey line is the hydrophilic pore energy at $V_{\text{applied}} = 0$ mV; yellow
11 through to red plots the reduction in free energy from 100 to 700 mV. Increasing the
12 applied potential difference is predicted to lower and broaden the local energy
13 minimum that supports the hydrophilic pore, and lower the barrier to unbounded pore
14 expansion.

15 **Fig. 2: Imaging electroporation.** (a) Cartoon of the DIB experimental setup. Contact
16 between a planar substrate and an aqueous droplet which both bear a self-assembled
17 lipid monolayer produces the bilayer. Expanded region indicates the location of the
18 bilayer and depicts a toroidal electropore, along with the direction of motion of Ca^{2+}
19 ions, enabling visualization of individual electropores by TIRF microscopy. (b) Pores
20 are observed as bright spots within the bilayer. The edge of the bilayer is indicated by
21 the dashed line. The image is the maximum pixel intensity of 40 frames recorded at
22 61.7 Hz at an applied potential of 485 mV. Scale bar: 10 μm . (c) When a single pore
23 is observed (160 mV), the electrical (upper) and fluorescence signals (lower)
24 correspond. *Upper images:* Frames at 32.9 Hz demonstrating only a single pore is

1 present. Scale bar: 25 μm . *Lower images*: Expanded views of the pores showing the
2 fluctuation in spot radius. Scale bar: 5 μm .

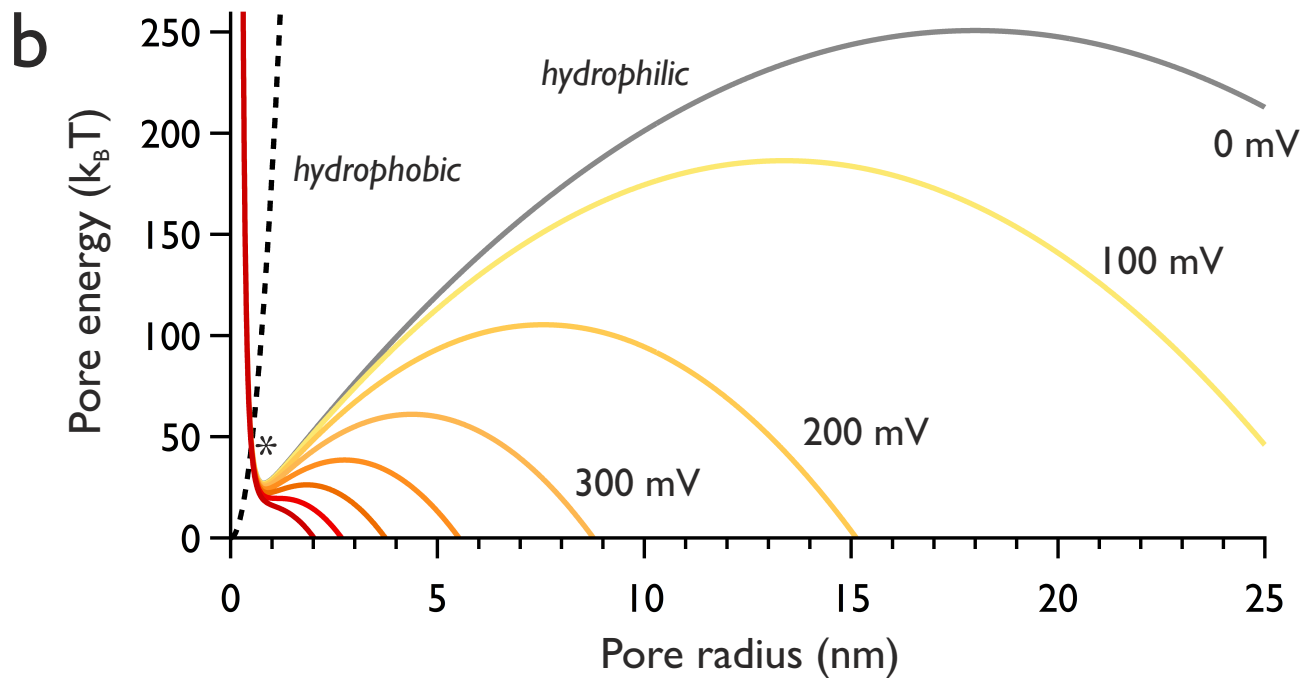
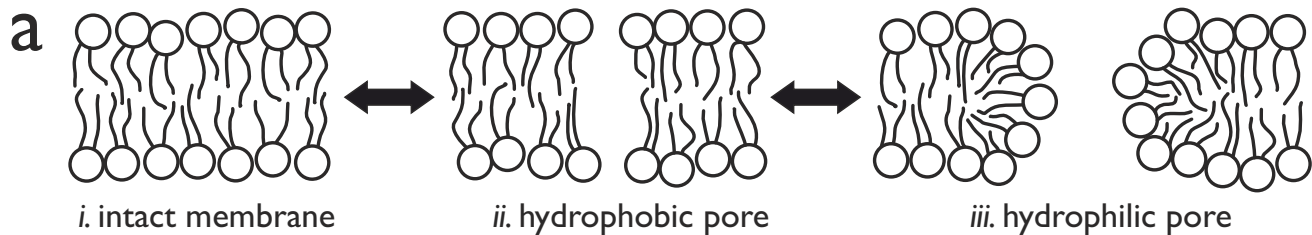
3 **Fig. 3: Ensemble response.** (a) Number and size of pores increases with voltage:
4 maximum intensity images from >1000-frame recordings on the same bilayer. Scale
5 bar: 25 μm . (b) Histograms of oSCR intensities for a single pore within a bilayer
6 experiencing an increasing applied potential. Pore amplitudes were obtained by 2D
7 Gaussian fitting to the oSCR spot throughout the 1000-frame movie. (c) Data from an
8 ensemble of spots ($n = 2424, 3137, 5641, 8411$ and 9428 respectively) as the potential
9 is varied.

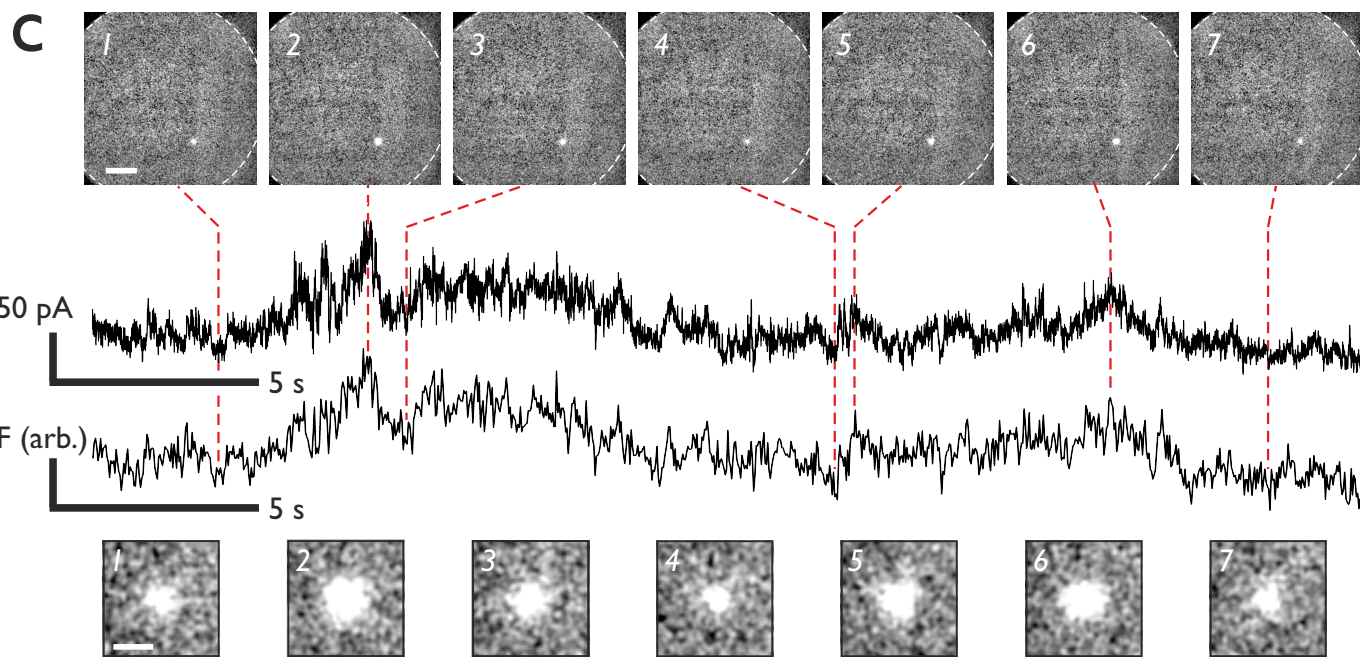
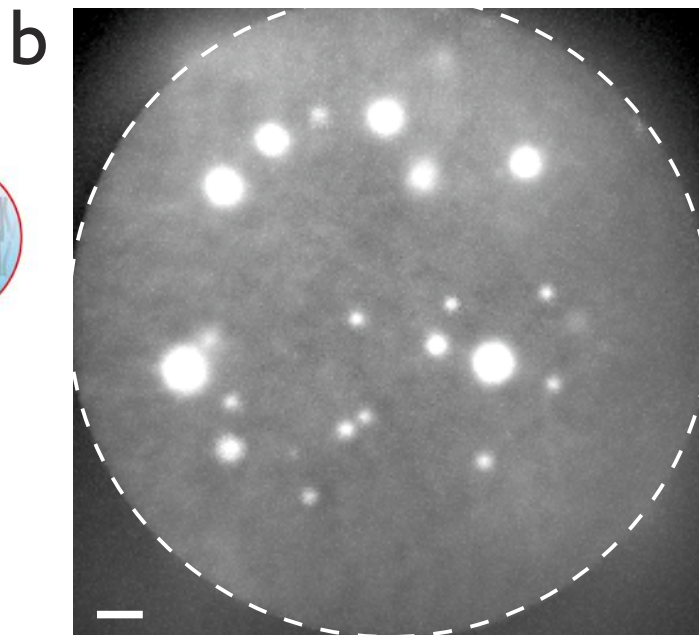
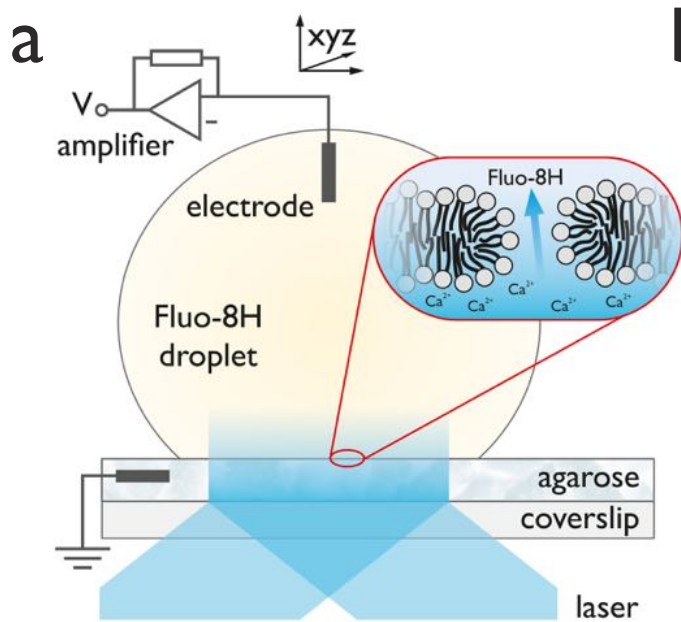
10 **Fig. 4: Electropore diffusion.** (a) A single frame from an oSCR stack (61.7 Hz) of a
11 diffusing electropore, recorded at 200 mV, overlaid with the tracking trajectory (blue,
12 0 s, to red, 16.2 s). The pink circle indicates the detected location of the spot in this
13 frame. Scale bar: 2 μm . (b) Representative mean-squared displacement versus time
14 plots. Open circles: 180 mV; filled squares: 200 mV; open lozenges: 260 mV; filled
15 triangles: 330 mV. Mean $D_{\text{lat}} = 0.67 \mu\text{m}^2 \text{s}^{-1}$ ($n = 46$). We observe no obvious
16 correlation of diffusivity with the applied potential. (c) Electroporation in a
17 DPhPC:DPPG:cholesterol (1:1:1) phase-separated DIB. Median image of 500 frames
18 recorded at 99.4 Hz. Electropores form in the (bright) L_d phase, diffusing around the
19 (dark) L_o regions. Colored overlays show the trajectories of different tracked
20 electropores. Scale bar: 5 μm .

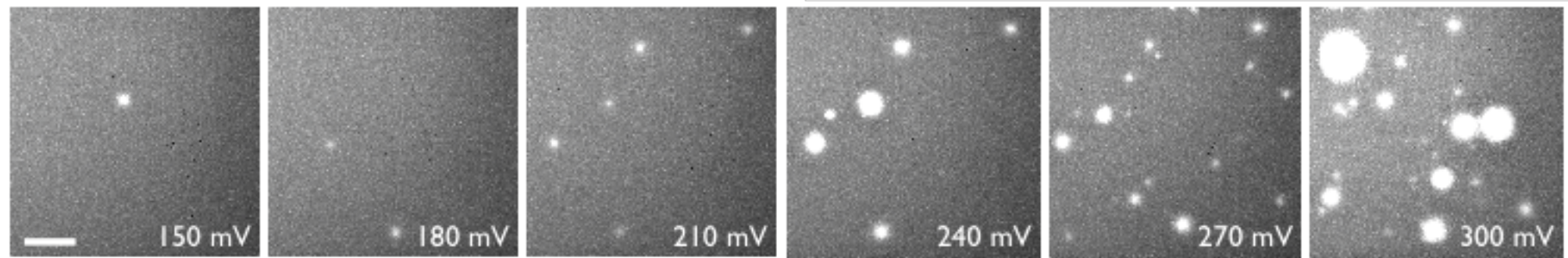
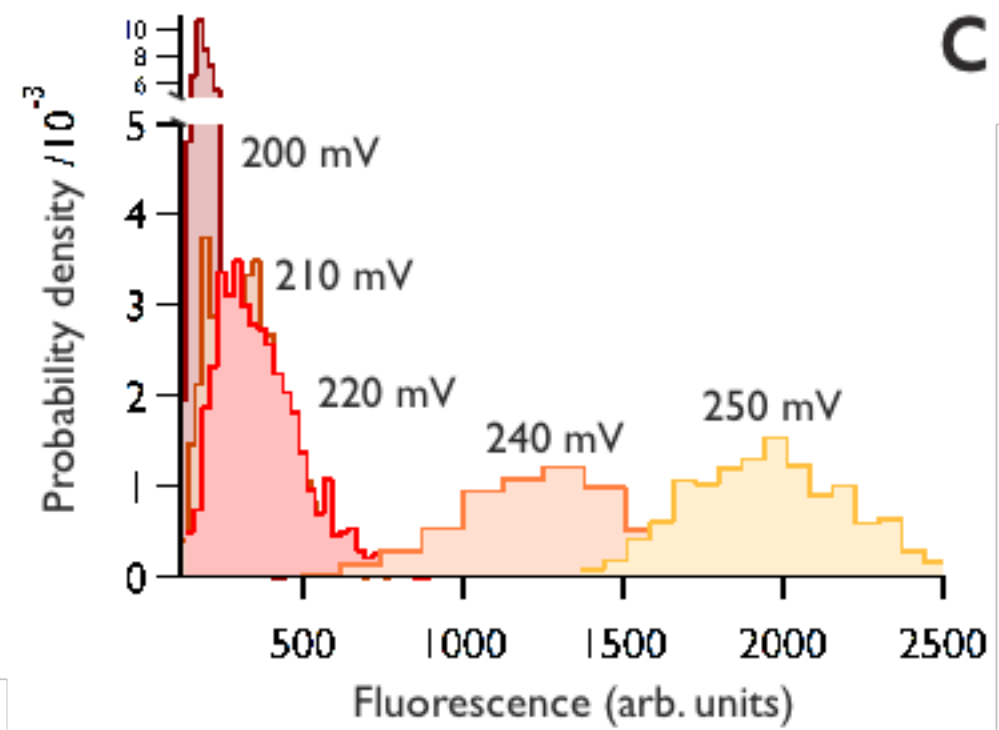
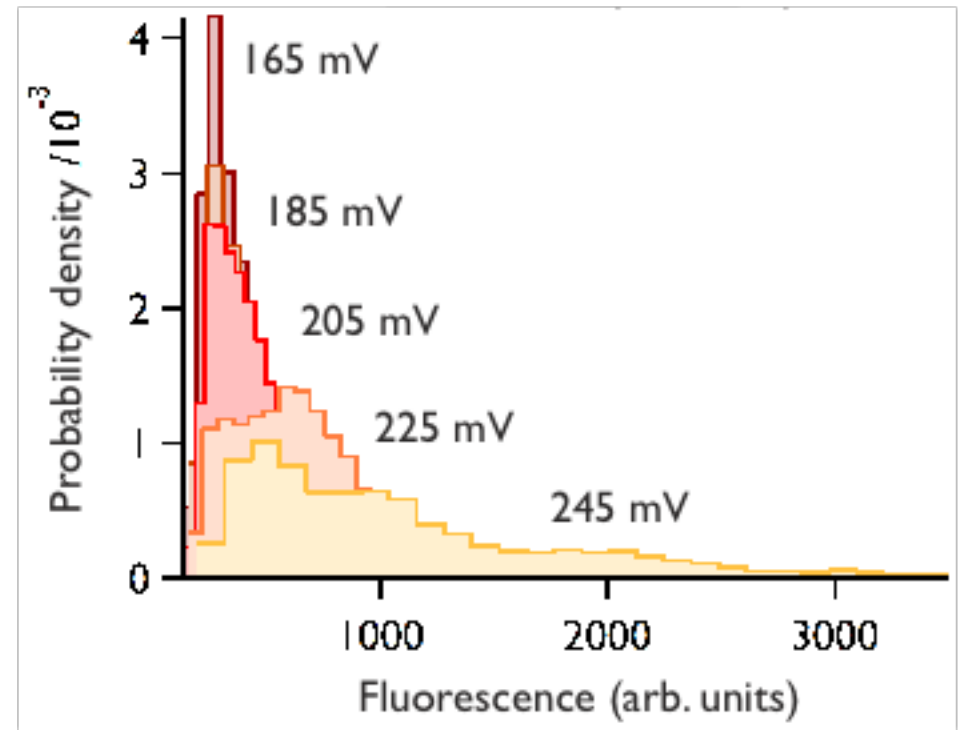
21 **Fig. 5: Rupture and cooperativity.** (a) Bilayers always rupture from a single pore.
22 Images show snapshots of rupture of a bilayer after irreversible expansion of a single
23 electropore at 200 mV. The dashed circle highlights the bilayer edge. Each image is a
24 100 ms exposure. (b) Two neighboring pores expand and contract in contrary motion.
25 Red and black lines plot the oSCR intensity for the right and left pores respectively.

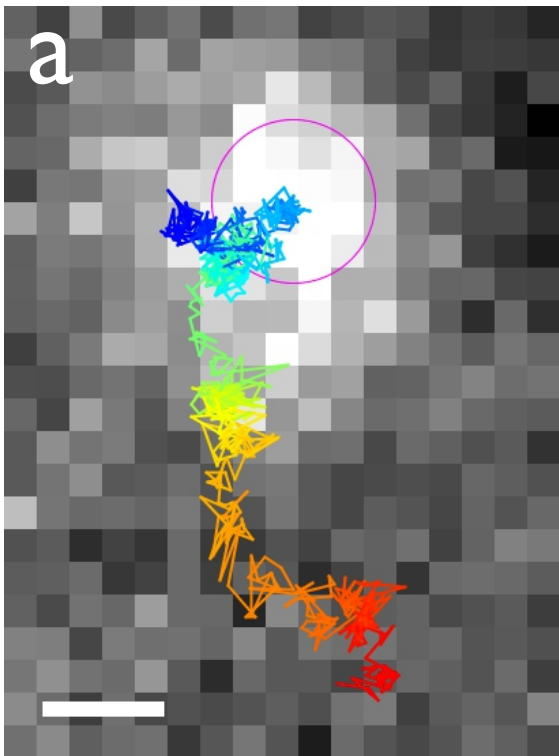
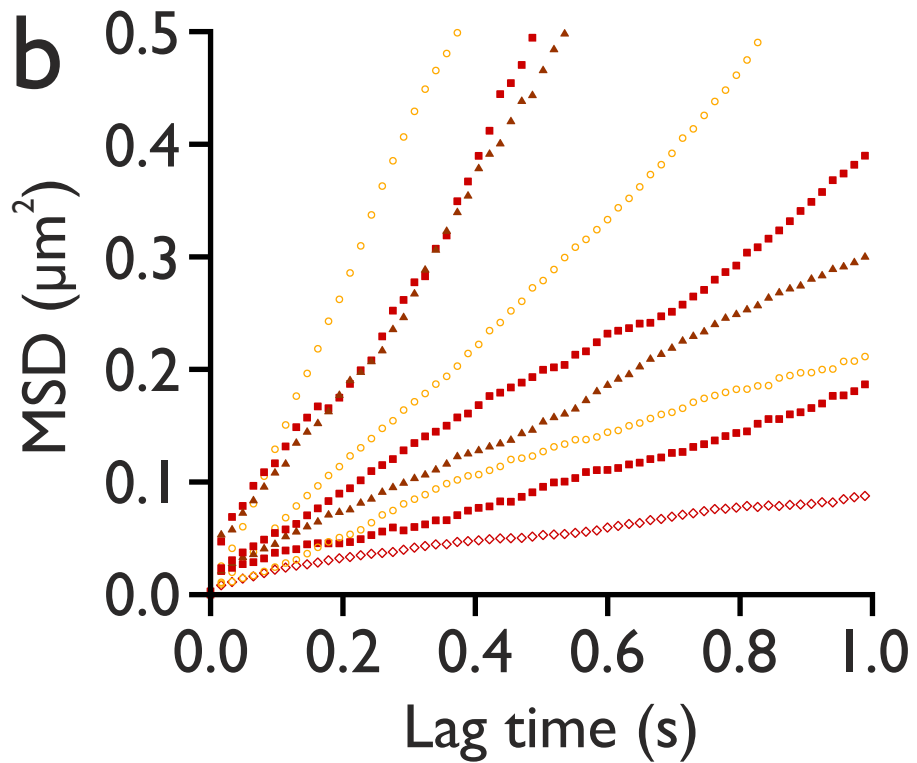
1 Images are 100 ms frames; their location in time with respect to the fluorescence data
2 is indicated by the dotted lines. Both scale bars are 25 μm .

3 **Fig. 6: Kinetics of small electropores.** (a) Fluctuating intensity of an isolated
4 electropore (black trace, upper) with detected open and closed states (red, lower). The
5 red dashed line is the threshold that defines the open and closed states, equal to 3σ of
6 the background fluctuations. (b) Representative histograms at both extremes of V_{applied}
7 showing exponential fits to the open and closed time distributions that exhibit two
8 decay constants. The applied potential was 260 mV for the open lifetime and 160 mV
9 for the closed lifetime histogram. (c) Electropore lifetimes vs. V_{applied} . Different
10 markers represent data from experiments carried out on different bilayers on different
11 days, but under identical experimental conditions. Number of pores analyzed ≥ 1900 .
12 Temporal resolution: 16.21 ms.





a**b****c**

a**b****c**